Title
Water Uptake and Proton Conductivity in Porous Block Copolymer Electrolyte Membranes

Journal
Macromolecules, 48(16)

ISSN
0024-9297

Authors
Chen, X Chelsea
Kortright, Jeffrey B
Balsara, Nitash P

Publication Date
2015-08-25

DOI
10.1021/acs.macromol.5b00950

Peer reviewed

Macromolecules

Article

pubs.acs.org/Macromolecules

Water Uptake and Proton Conductivity in Porous Block Copolymer Electrolyte Membranes

X. Chelsea Chen,[†] Jeffrey B. Kortright,[†] and Nitash P. Balsara*[,†,‡,§]

[†]Materials Sciences Division and [‡]Energy Technologies Area, Lawrence Berkeley National Laboratory, Berkeley, California 94720, United States

[§]Department of Chemical and Biomolecular Engineering, University of California, Berkeley, Berkeley, California 94720, United States

Supporting Information

ABSTRACT: We demonstrate that the water uptake and conductivity of proton-conducting block copolymer electrolyte membranes can be controlled systematically by the introduction of pores in the conducting domains. We start with a membrane comprising a mixture of homopolymer polystyrene (hPS) and a polystyrene-*b*-polyethylene-*b*-polystyrene (SES) copolymer. Rinsing the membranes in tetrahydrofuran and methanol results in the dissolution of hPS, leaving behind a porous membrane. The polystyrene domains in the porous SES membranes are then sulfonated to give a porous membrane with hydrophilic and hydrophobic domains. The porosity is controlled by controlling ϕ_v, the volume fraction of hPS in the blended membrane. The morphology of the membranes before and after sulfonation was studied by scanning transmission electron microscopy (STEM), electron tomography, and resonance soft X-ray scattering (RSoXS). The porous structures before and after sulfonation are qualitatively different. Water uptake of the sulfonated membranes increased with increasing ϕ_v. Proton conductivity is a nonmonotonic function of ϕ_v with a maximum at $\phi_v = 0.1$. The introduction of microscopic pores in the conducting domain provides an additional handle for tuning water uptake and ion transport in proton-conducting membranes.

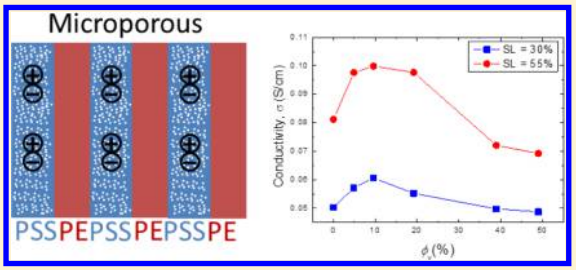

INTRODUCTION

Polymer electrolyte membranes (PEMs) have broad applications in clean energy and water-related technologies such as fuel cells, redox flow cells, electrodialysis, and reverse osmosis.[1−3] These nonporous membranes comprise nanoscale hydrophilic and hydrophobic domains. The hydrophilic domains, which usually contain sulfonic acid groups, get swollen in the presence of water and provide avenues for proton transport. The hydrophobic domains remain dry and provide the membrane with mechanical integrity.[4−7] Water uptake in these systems is governed by the nature of the hydrophilic domains as well as stresses created in the membrane due to swelling of the hydrophilic domains. Mesoporous inorganic membranes such as porous silica wherein the pores are lined with sulfonic acid groups provide another approach for enabling proton transport.[8] In these systems, water-filled pores provide avenues for proton transport. Because of the rigid nature of inorganic materials (the tensile modulus of silica is about 37 GPa), the sizes of the hydrophilic and hydrophobic domains are unlikely to be affected by stresses generated by the absorption of water.

In this paper, we study porous polymer electrolyte membranes. The introduction of pores provides additional control over water uptake. We start with a membrane comprising a mixture of homopolymer polystyrene (hPS) and a polystyrene-*b*-polyethylene-*b*-polystyrene (SES) copolymer. Rinsing the membranes in tetrahydrofuran and methanol results in the dissolution of hPS, leaving behind a porous membrane. The polystyrene domains in the porous SES membranes are then sulfonated to give a porous membrane with hydrophilic and hydrophobic domains. The porosity is controlled by controlling the volume fraction of hPS in the blended membrane. We thus obtain membranes that are chemically identical, differing only in pore volume fraction. The morphology of the membranes before and after sulfonation was studied by scanning transmission electron microscopy (STEM), electron tomography, and resonance soft X-ray scattering (RSoXS). We quantify the effect of the porous structure on water uptake and proton conductivity. This paper is part of the series on the interplay between morphology, porosity, solvent uptake, and ion transport through block copolymer electrolyte membranes.[9−14]

EXPERIMENTAL SECTION

Synthesis and Characterization of Polymers. Homopolymer polystyrene was synthesized by anionic polymerization using *sec*-butyllithium as the initiator. Polystyrene-*b*-polybutadiene block copolymer was synthesized by sequential anionic polymerization of styrene and butadiene, using *sec*-butyllithium as the initiator. Polystyrene-*b*-polybutadiene was coupled using dibromoethane to yield a symmetric polystyrene-*b*-polybutadiene-*b*-polystyrene (SBS) triblock copolymer.[15] SBS was hydrogenated using *p*-toluenesulfonyl

Received: May 4, 2015
Revised: July 3, 2015
Published: August 10, 2015

DOI: 10.1021/acs.macromol.5b00950
Macromolecules 2015, 48, 5648−5655

hydrazide in the presence of equimolar tri-*n*-propylamine to yield SES. Our synthesis approach is described in ref 14.

The molecular weight of the polystyrene blocks of the SBS copolymer was obtained by drawing aliquots of the reaction mixture before addition of butadiene, terminating the living anions with methanol, and conducting gel permeation chromatography (GPC) experiments on a Viscotek GPC Max VE-2001 equipped with a TDA 302 triple-detector system, calibrated using polystyrene standards with tetrahydrofuran (THF) as the eluent. The molecular weight of the polybutadiene (PB) block of the SBS copolymer and the ratio of 1,4-addition to 1,2-addition in the PB blocks of the copolymer were determined using ^{1}H nuclear magnetic resonance (NMR) spectroscopy ($CDCl_3$, 25 °C). High temperature NMR (toluene-d_8, 90 °C) was used to ensure the complete saturation of the vinyl groups in the polybutadiene block of SBS to yield SES. The dispersities of hPS and SBS were 1.06 and 1.02, based on polystyrene standards. The characteristics of hPS and SES are given in Table 1.

Table 1. Physical Characteristics of Polymers Used in This Work

polymer	PS M_n (kg/mol)	PE M_n (kg/mol)	PS vol fraction
hPS	5.9	–	1
SES	13.8	37.4	0.41

Membrane Preparation and Sulfonation. Predetermined ratios of hPS and SES were dissolved in *o*-xylene and gently stirred at 100 °C for 4 h. The solution was then cast on an ultraclean aluminum foil using a custom-built solvent caster equipped with a doctor blade at 80 °C. The concentration of the solution and the height of the doctor blade were adjusted to obtain membranes with thicknesses of 40 ± 5 μm. The membranes were dried under vacuum at 80 °C for 24 h. After drying, the aluminum foil was removed by immersing the membrane (with the aluminum foil stuck to it) in 1 M hydrochloric acid. The resulting free-standing membrane was washed with deionized water several times and dried under vacuum for 16 h.

The free-standing hPS/SES blend membranes were washed with THF at room temperature, to selectively dissolve hPS, followed by a methanol rinse. This is repeated three times to ensure complete removal of hPS. The weight of the membranes before and after washing was measured. For all the membranes used in the study, the weight of hPS originally blended into SES was equal to the weight extracted. We define the nominal pore volume fraction, ϕ_v, as the volume fraction of hPS that was blended with SES and subsequently extracted.

Pristine nonporous SES membranes were prepared following the same steps described above for systematic comparison (acid wash followed by THF/methanol rinses).

SES membranes (porous and nonporous) were sulfonated in a custom-designed three-neck reactor. A membrane with 2 in. diameter was punched out and held in place with a custom-designed Teflon clamp inside the reactor. The sulfonation reaction was conducted in 1,2-dichloroethane with acetic sulfate as the sulfonating agent, as reported previously.[14] The sulfonated membranes (S-SES) were stored in deionized water prior to measurements.

The membrane fabrication process is schematically shown in Figure 1.

Determination of Ion Content. Ion exchange capacity (IEC), defined as the milliequivalents of sulfonic acid groups per dry gram of polymer (mmol/g), was measured using the following procedure:[16] a piece of water-equilibrated membrane was immersed in 1 M NaCl and gently stirred for 16 h. During this time, the H^+ ions in the membrane are replaced by Na^+ ions. After completion of ion exchange, membrane was removed from the solution. The solution was titrated with a standard 0.01 M NaOH solution to the phenolphthalein end point. The membrane was then soaked in 0.1 M HCl for 2 h to return it to the acid form. After acid treatment, the membrane was washed with deionized water several times and soaked in deionized water for 16 h. Finally the membrane was dried under vacuum at room temperature

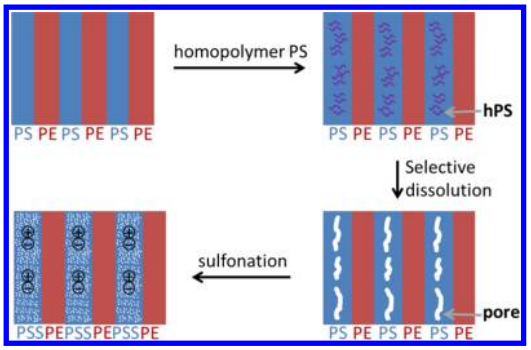

Figure 1. Fabrication of porous block copolymer electrolyte membranes. The process includes casting membranes with hPS/SES blends of different volume ratios, followed by selective dissolution of hPS, creating a mesoporous SES membrane with pores lined with the PS phase. The porous SES membrane is subsequently sulfonated as one piece in a custom-made reactor, where the PS blocks of SES are sulfonated.

for 24 h and then at 80 °C for 2 h. It was allowed to cool down in a desiccator before the dry weight, W_{dry}, was measured. IEC is calculated using eq 1.

$$\text{IEC (mmol/g)} = \frac{\text{vol of NaOH soln (mL)} \times \text{concn of NaOH soln (M)}}{W_{dry}\ \text{(g)}} \quad (1)$$

The sulfonation level (SL) of S-SES, defined by eq 2, was calculated from IEC and the weight fraction of PS block in SES.

$$\text{SL} = \frac{\text{mol SSA}}{\text{mol S} + \text{mol SSA}} \times 100\% \quad (2)$$

where SSA is styrenesulfonic acid and S is styrene.

Morphology of the Membranes. Morphology of the membranes was characterized with scanning transmission electron microscopy (STEM), STEM tomography, and resonance soft X-ray scattering (RSoXS).

STEM and STEM Tomography. SES samples were prepared by microtoming hPS/SES blend using a Leica EM FC6 at −120 °C, followed by washing the thin microtomed sections with THF and methanol. S-SES samples were obtained by directly microtoming S-SES membranes at −120 °C. The thickness of the samples was approximately 70 nm. STEM experiments were performed on a Tecnai F20 UT FEG, equipped with a high angle annular dark field (HAADF) detector, using 200 keV acceleration voltage. SES samples were stained in RuO_4 vapor for 30 min prior to STEM measurements. S-SES samples were not stained.

For STEM tomography, gold nanoparticles with 10 nm diameter were deposited on the sample to facilitate alignment of the tilt series images. Tomography experiments were performed on a FEI Titan microscope using 200 keV acceleration voltage. Single tilt series images were collected in the angle range −70° to 70° for each tilt series. Exposure time for image collection was set to 10 s. Alignment and reconstruction were done using the IMOD tomographic reconstruction software package. The reconstructed tomogram was segmented and colored using Avizo Fire.

RSoXS Measurements. RSoXS experiments were performed at Beamline 11.0.1.2 at the Advanced Light Source (ALS) at Lawrence Berkeley National Laboratory (LBNL). Free-standing SES membranes were mounted onto a sample holder and loaded into the RSoXS chamber. S-SES membranes were removed from water and spread on a silicon nitride window substrate with a window thickness of 200 nm and dried in a vacuum oven overnight before loading into RSoXS chamber. Samples used for RSoXS experiments were approximately 6 μm. Data were analyzed using a modified version of the Nika program.[17] The original two-dimensional scattering images were azimuthally averaged to generate one-dimensional scattering intensity

DOI: 10.1021/acs.macromol.5b00950
Macromolecules 2015, 48, 5648−5655

profiles, $I(q)$. The scattering wave vector $q = 4\pi \sin(\theta/2)/\lambda$, where θ is scattering angle and λ is the wavelength of the incident beam.

Water Uptake and Dimensional Change. Water uptake, WU, of the membranes is defined by eq 3

$$\mathrm{WU} = \frac{W_{\mathrm{wet}} - W_{\mathrm{dry}}}{W_{\mathrm{dry}}} \times 100\% \tag{3}$$

where W_{wet} is the wet weight of the membranes and W_{dry} is the dry weight of the membranes. Dimensional change, ΔV, of the membranes is defined by eq 4

$$\Delta V = \frac{V_{\mathrm{wet}} - V_{\mathrm{dry}}}{V_{\mathrm{dry}}} \times 100\% \tag{4}$$

where V_{wet} is the wet volume of the membranes and V_{dry} is the dry volume of the membranes. To obtain W_{wet} and V_{wet}, a piece of water-equilibrated circular membrane was punched out and gently dabbed with a KimWipe to remove surface water. The weight of the membrane was then quickly measured on a balance. The wet volume was measured by measuring the diameter of the membrane with a caliper and measuring the thickness of the membrane with a micrometer. The membrane was subsequently dried under vacuum at room temperature for 24 h and then at 80 °C for 2 h. It was allowed to cool down in a desiccator before W_{dry} and V_{dry} were measured.

The hydration number, λ, specified as the number of water molecules per sulfonic acid group, was calculated from WU and IEC of S-SES, as given by eq 5, where $\mathrm{MW_{H_2O}} = 18.02$ g/mol.

$$\lambda = \frac{[\mathrm{H_2O}]}{[\mathrm{SO_3^-}]} = \frac{\mathrm{WU}\ (\%) \times 10}{\mathrm{MW_{H_2O}} \times \mathrm{IEC}} \tag{5}$$

Proton Conductivity. In-plane proton conductivity of membranes equilibrated in liquid water, with a dimension of 2 cm × 1 cm, was measured at 25 °C in water by ac impedance spectroscopy in the standard four-probe configuration using a BekkTech sample clamp with platinum electrodes. Data were collected over a frequency range of 1 Hz−100 kHz. Proton conductivity, σ, is given by eq 6

$$\sigma = \frac{l}{whR} \tag{6}$$

where w and h are the width and the thickness of the membranes, respectively, R is the touchdown of the Nyquist semicircle on the real axis, and l is the distance between the inner platinum electrodes.

RESULTS AND DISCUSSION

We begin by reviewing the membrane fabrication process. In previous studies,[15,18] we have shown that adding hPS to an SES copolymer and selectively dissolving it results in a mesoporous morphology as shown schematically in Figure 1. However, it is difficult to predict the morphology of membranes after sulfonation. The molar volume occupied by polystyrene sulfonate (PSS) monomers is 141.8 $\mathrm{cm^3}$/mol, larger than that occupied by PS monomers, 100.6 $\mathrm{cm^3}$/mol, both calculated using the group contribution method.[19] Thus, complete sulfonation of PS chains will lead to a 40.9% volume increase of the PS domains, corresponding to 16.8% volume increase of the entire SES membrane. Therefore, after sulfonation, the volume of S-SES membrane increases, and concurrently some of the pore volume in porous S-SES will be taken up by the PSS chains. The semicrystalline PE domains may deform during the sulfonation step, and this can also affect pore volume.[20] In Figure 1, we show that the PSS domains in the S-SES membrane have tiny pores. Justification for this is given toward the end of this paper.

We focus on six membranes described in Table 2. We refer to the unsulfonated membranes as SES(x) and the sulfonated membranes as S-SES(x), where x, the volume percent of hPS that was blended with SES and subsequently extracted, is the nominal pore volume percent. The morphology of SES and S-SES membranes described in Table 2 was studied by STEM and RSoXS. Note that the morphological studies throughout this work were done on membranes in the dry state. Scanning transmission electron microscopy images of SES membranes collected in HAADF mode are shown in Figure 2a−c. These samples were stained with $\mathrm{RuO_4}$ vapor, which stains the PS component in SES. SES(0) presented a lamellar morphology, as shown in Figure 2a. The bright domains are PS-rich domains. In SES(10) and SES(40), dark domains with length scales between 10 and 30 nm are observed, as shown in Figure 2b,c. We examined SES(10) and SES(40) membranes prior to

Table 2. Samples Used for Morphology Study

sample code	ϕ_v[a]	IEC (mmol/g)	SL (%)
SES(0)	0	0	0
SES(10)	0.096	0	0
SES(40)	0.39	0	0
S-SES(0)	0	2.25	67.3
S-SES(10)	0.096	2.16	64.0
S-SES(40)	0.39	1.61	45.5

[a] ϕ_v is equal to volume fraction of hPS that was blended with SES and subsequently extracted.

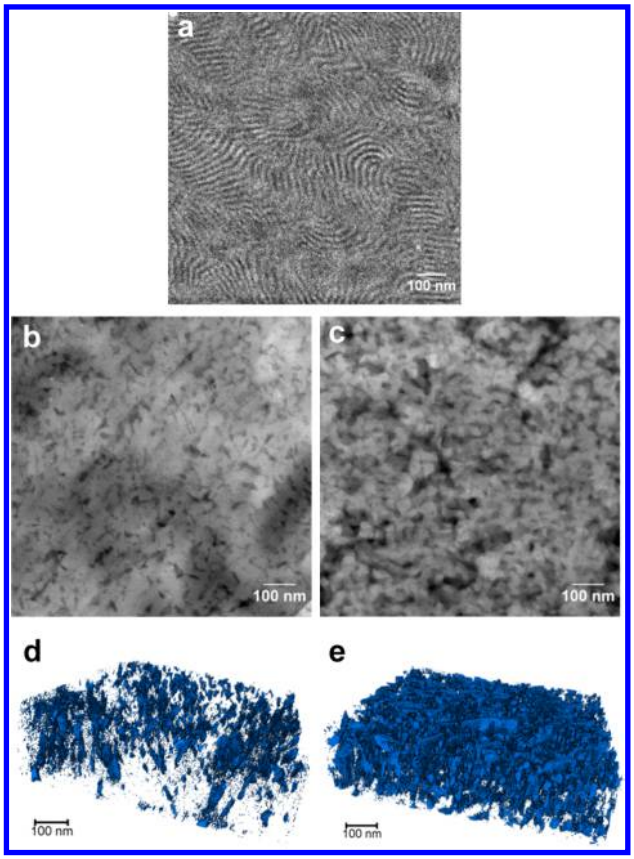

Figure 2. Morphology of SES membranes. (a−c) STEM images of SES(0), SES(10), and SES(40) respectively. Samples were stained with $\mathrm{RuO_4}$. In (a), bright domains represent PS-rich phase and dark domains represent PE-rich phase. In (b) and (c), bright domains represent polymer and dark domains represent pores. (d, e) STEM tomograms of SES(10) and SES(40). Blue segementaions in (d) and (e) represent pores.

DOI: 10.1021/acs.macromol.5b00950
Macromolecules 2015, 48, 5648−5655

washing out hPS. The STEM images obtained from these samples did not show the dark features seen in Figure 2b,c (STEM images not shown for brevity). We conclude that the dark features seen in Figure 2b,c represent mesoscale pores in SES(10) and SES(40) created by the washing process. The strong contrast between pores and polymer precludes characterization of microphase separation between PS and PE domains. Three-dimensional tomograms of SES(10) and SES(40) highlighting pores are shown in Figure 2d,e. The blue segmentations represent pores, which corresponds to the dark regions in Figure 2b,c. The pores in SES(10) appear ellipsoidal and isolated. The pores in SES(40) appear slit-shaped and connected. It is qualitatively evident from Figure 2 that pore fraction increases as ϕ_v increases. Calculating an absolute pore fraction from STEM tomograms is difficult, as there is lack of a clean threshold necessary to distinguish pores from polymer in the micrographs. The thresholding used in Figure 2d,e gives a pore fraction of 0.076 for SES(10) and 0.33 for SES(40). It is evident that the ratio of pore fractions 4.3 = 0.33/0.076 is in reasonable agreement with the expected value of 4.0. It is worth mentioning that the porous structure seen in Figure 2 was only observed when the hPS/SES blend was first microtomed followed by washing the microtomed sections with THF and methanol. When we directly microtomed porous SES samples, the pores collapsed during the microtoming process even though cryogenic conditions were used.

The phase behavior of mixtures of homopolymer A and an A−B diblock copolymer has been extensively studied.[21−23] In a previous study in our group, we systematically examined the morphology of hPS/SES mixtures as a function of α, the ratio of the molecular weight of homopolymer PS (hPS) to that of the PS block (bPS) in SES copolymer.[15,18] Three regimes were identified in ref 18: when $\alpha < 0.22$, hPS is miscible with both bPS and PE blocks of SES; when $0.22 < \alpha < 0.90$, hPS resides in bPS phase; when $\alpha > 0.90$, hPS macrophase separates from SES. These results are consistent with theoretical calculations.[24,25] In the study presented herein, we chose $\alpha = 0.43$, in the regime where hPS selectively mixes with bPS but not PE, as schematically shown in Figure 1. The pores created by selective extraction of hPS from hPS/SES should thus be templated in the PS-rich phase. STEM experiments confirmed the presence of pores, but due to the strong contrast between polymer and pores, we cannot discern the contrast between PS-rich and PE-rich microphases.

After sulfonation, S-SES(0) maintained the lamellar morphology, as shown in Figure 3a. The S-SES samples in Figure 3 were not stained. The bright domains represent sulfur-rich PSS domains. The high electron density of sulfur atoms results in natural contrast in S-SES membranes. S-SES(10) also presented a similar lamellar morphology to S-SES(0) (Figure 3b). S-SES(40) showed a bicontinuous structure (Figure 3c). Mesoscale pores are not observed in the STEM images of S-SES(10) and S-SES(40). Energy-dispersive X-ray spectroscopy (EDS) analysis of S-SES(0) and S-SES(40) presented in the Supporting Information, Figures S1 and S2, supports this observation. This suggests that mesoscale pores in SES(10) and SES(40) membranes may have been filled during the sulfonation reaction.

Figure 4 shows the physical appearance of SES(40) and S-SES(40). SES(40) is opaque whereas S-SES(40) is transparent, consistent with our conclusion that mesoscale pores are present in SES(40) but not in S-SES(40).

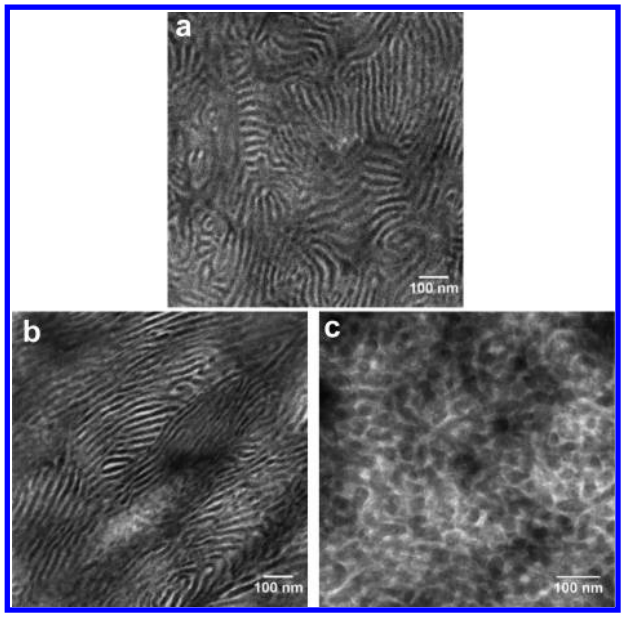

Figure 3. Morphologies of S-SES(0) (a), S-SES(10) (b), and S-SES(40) (c) shown by STEM. Samples were unstained. Bright domains represent the PSS-rich phase, and dark domains represent the PE-rich phase.

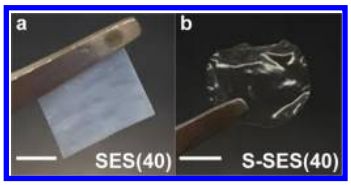

Figure 4. (a) Physical appearance of SES(40). (b) Physical appearance of S-SES(40). Scale bar represents 0.5 mm.

Resonance soft X-ray scattering was used to complement STEM characterizations. In RSoXS, the scattering contrast between different components, $C_{i,j}$, is a function of the X-ray energy,[26,27] $h\nu$, as depicted in Figure 5a,b; i, j = PS, PSS, PE, or pores. $C_{i,j} = (n_i - n_j)^2$, where n_i and n_j are the refractive indices of components i and j, respectively. The refractive indices of PS, PSS, and PE are calculated using the method described in ref 18. Traditional hard X-ray scattering contrast is dominated by the contrast between polymers and pores, as seen in Figure 5 when $h\nu = 300$ eV. RSoXS scattering contrasts in the vicinity of the carbon K edge (284.2 eV) are qualitatively different from that obtained in hard X-ray scattering. The RSoXS scattering profiles from porous SES membranes are governed by the contrast between PE and PS, $C_{PE,PS}$, that between PE and pores, $C_{PE,pore}$, and that between PS and pores, $C_{PS,pore}$. (For simplicity, we treat PE as a single component in spite of the fact that it is a semicrystalline polymer comprising amorphous and crystalline regions.) As Figure 5a depicts, when $h\nu$ is 278.7 eV, $C_{PE,pore} \approx C_{PE,PS} \gg C_{PS,pore}$, indicating that at this energy the RSoXS signal is dominated by PE−pore and PE−PS contrasts. When $h\nu$ is 285.0 eV, $C_{PE,PS} \approx C_{PS,pore} \gg C_{PE,pore}$. If there are no pores, then the RSoXS profiles at both 278.7 and 285.0 eV would be dominated by $C_{PE,PS}$. In other words, RSoXS profiles that are independent of $h\nu$ imply the absence of pores. Conversely, qualitative differences between RSoXS profiles at 278.7 and 285.0 eV indicate the presence of pores. Similarly, RSoXS scattering profiles from porous S-SES membranes are governed by the contrast between PE and PSS, $C_{PE,PSS}$, that between PE

DOI: 10.1021/acs.macromol.5b00950
Macromolecules 2015, 48, 5648−5655

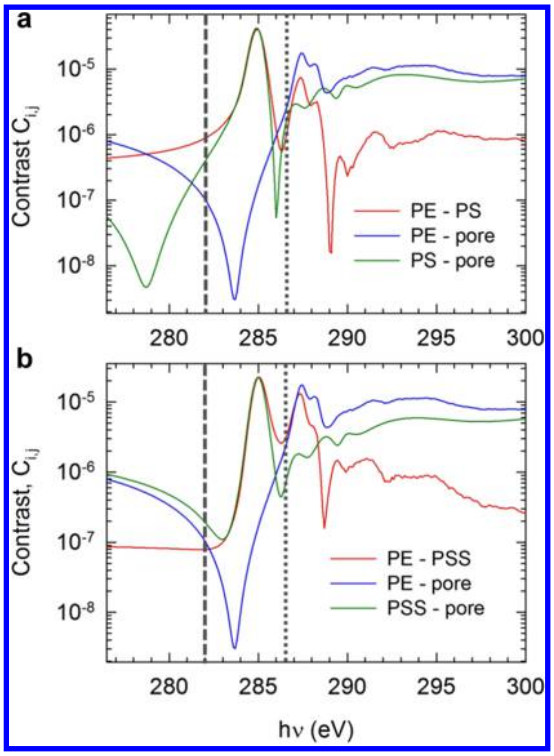

Figure 5. Contrast, $C_{i,j}$, as a function of the X-ray energy, $h\nu$, in SES and S-SES membranes (a and b, respectively). Vertical dashed lines in (a) and (b) represent $h\nu$ = 280.0 eV. Vertical dotted lines in (a) and (b) represent $h\nu$ = 284.6 eV. These lines are used for Figures 6 and 7.

and pores, $C_{PE,pore}$, and that between PSS and pores, $C_{PSS,pore}$. As shown in Figure 5b, when $h\nu$ is 278.7 eV, $C_{PE,pore} \approx C_{PSS,pore} \gg C_{PE,PSS}$. Note that changing PS to PSS results in a qualitative change in contrasts at 278.7 eV: in SES the PS−pore contrast is negligible while in S-SES the PE−PSS contrast is negligible. When $h\nu$ is 285.0 eV, $C_{PE,PSS} \approx C_{PSS,pore} \gg C_{PE,pore}$, for S-SES membranes (Figure 5b), which is similar to SES membranes.

We begin by describing RSoXS profiles of SES membranes at $h\nu$ = 280.0 and 284.6 eV. These two energies are indicated in Figures 5a and 5b as vertical dashed and dotted lines, respectively. We did not choose $h\nu$ = 285.0 eV, the X-ray energy that gives the maximum contrast difference; instead, we chose to use 284.6 eV. This is because of strong X-ray absorption at the carbon K edge, the RSoXS signal collected at 284.6 eV has higher signal-to-noise ratio than at 285.0 eV. RSoXS intensities as a function of the magnitude of the scattering wave vector, q, at these energies for SES membranes are shown in Figure 6. For SES(0) (Figure 6a), there appears to be no significant difference between the scattering profile at $h\nu$ = 280.0 eV and that at $h\nu$ = 284.6 eV, both showing a single broad peak at q^*_{SES0} = 0.18 nm^{-1}. This is expected, because there are no mesoscale pores in SES(0) and scattering contrast at these two energies is given by $C_{PE,PS}$. The semicrystalline nature of the PE microphase and the contrast between amorphous and crystalline PE regions may be responsible for the low q upturn seen at 280.0 eV in SES(0). The characteristic length scale in SES(0), $d_{SES0} = 2\pi/q^*_{SES0}$, is calculated to be 34.3 nm, consistent with the lamellar spacing obtained from STEM (Figure 2a). In SES(10), scattering profiles at $h\nu$ = 280.0 eV and at $h\nu$ = 284.6 eV are quite different, as shown in Figure 6b. At $h\nu$ = 280.0 eV, SES(10) presented a single broad peak, at q^*_{SES10} = 0.17 nm^{-1}, corresponding to d_{SES10} = 37.0 nm, a slight increase relative to d_{SES0}. At $h\nu$ = 284.6 eV, we observe a broad scattering feature that appears to be a convolution of two peaks: a primary peak at q = 0.19 nm^{-1} and a secondary peak at q = 0.31 nm^{-1}. Based on arguments presented in the preceding paragraph, the qualitative difference between the $h\nu$ = 280.0 eV and $h\nu$ = 284.6 eV profiles seen in Figure 6b indicates the presence of a mesoporous structure in SES(10). In SES(40), the scattering profiles at $h\nu$ = 280.0 eV and at $h\nu$ = 284.6 eV differ dramatically from each other, as shown in Figure 6c. The scattering profile at $h\nu$ = 280.0 eV contains a shoulder at q^*_{SES40} = 0.15 nm^{-1}, similar to that obtained from bicontinuous microemulsions.[28,29] In contrast, the scattering profile at $h\nu$ = 284.6 eV contains a well-defined peak at q = 0.24 nm^{-1} and a minimum at q = 0.15 nm^{-1}. The qualitative differences in scattering profiles in Figure 6c confirm the presence of a mesoporous structure in SES(40). The RSoXS profiles of SES(0) and SES(10) at $h\nu$ = 280.0 eV indicate the presence of microphase-separated morphologies, consistent with the STEM images of these two samples (Figure 2a,b). The RSoXS profile of SES(40) at $h\nu$ = 280.0 eV indicates the presence of a bicontinuous microemulsion morphology, which is also consistent with the STEM image from this sample (Figure 2c). The lack of a position-space image that is sensitive to the microphase separation between PS and PE precludes definitive interpretation of the RSoXS profiles at $h\nu$ = 284.6 eV.

RSoXS intensities as a function of q at $h\nu$ = 280.0 eV and at $h\nu$ = 284.6 eV for S-SES membranes are shown in Figure 7. There are no differences between RSoXS profiles at $h\nu$ = 280.0

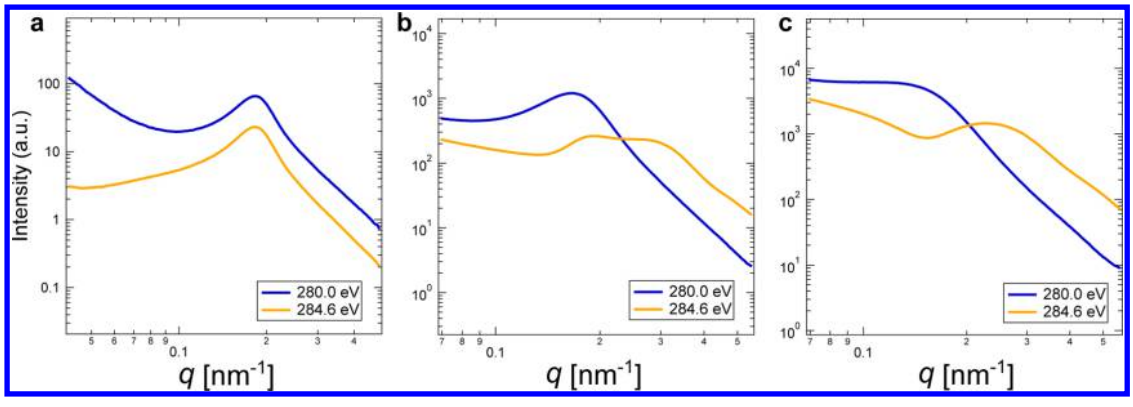

Figure 6. RSoXS intensity, as a function of the magnitude of scattering vector, q, for SES(0) (a), SES(10) (b), and SES(40) (c). For each sample, two X-ray energies were chosen, as indicated by the two vertical lines in Figure 5a. Scattering profiles are vertically shifted for the ease of comparison.

DOI: 10.1021/acs.macromol.5b00950
Macromolecules 2015, 48, 5648−5655

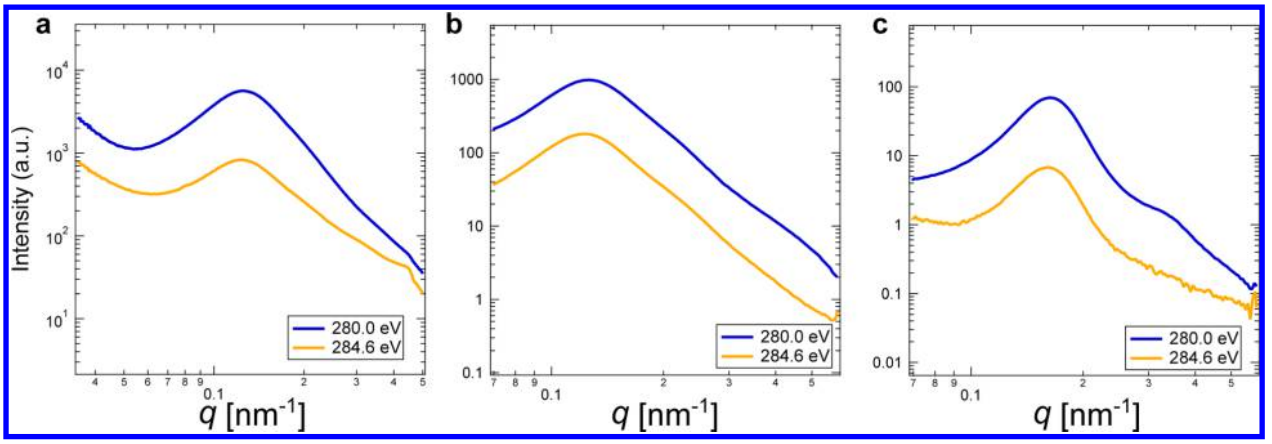

Figure 7. RSoXS intensity, as a function of the magnitude of scattering vector, q, for S-SES(0) (a), S-SES(10) (b), and S-SES(40) (c), respectively. For each sample, two X-ray energies were chosen, as indicated by the two vertical lines in Figure 5b. Scattering profiles are vertically shifted for the ease of comparison.

eV and at $h\nu$ = 284.6 eV for all three membranes: S-SES(0), S-SES(10), and S-SES(40), as shown in Figures 7a, 7b, and 7c, respectively. Therefore we conclude that a mesoporous structure is absent in S-SES membranes. To demonstrate that our conclusions are not based on the particular energies chosen in Figures 6 and 7, we plot RSoXS intensity of SES(10) at q^*_{SES10} = 0.17 nm^{-1} and $2q^*_{SES10}$ = 0.34 nm^{-1} as a function of $h\nu$ in Figure 8a. To do this, we normalized scattering spectra by the transmission spectra to correct for different absorption by different samples. Figure 8b shows the same type of plot for S-SES(10). When pores are absent (S-SES(10) in Figure 8b), the two curves are vertically displaced from each other. When pores are present (SES(10) in Figure 8a), the two curves are qualitatively different from each other. The RSoXS results are consistent with STEM results in Figures 2 and 3.

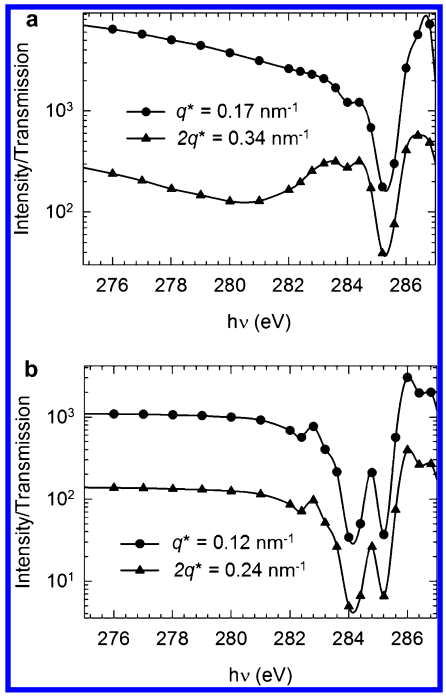

Figure 8. (a) RSoXS intensity normalized by transmission absorption, as a function of X-ray energy, $h\nu$, for SES(10). Two q values were chosen: q^* = 0.17 nm^{-1} and $2q^*$ = 0.34 nm^{-1}. (b) RSoXS intensity normalized by transmission absorption, as a function of $h\nu$, for S-SES(10). Two q values were chosen: q^* = 0.12 nm^{-1} and $2q^*$ = 0.24 nm^{-1}.

Having determined the morphologies of the S-SES membranes, we now move on to their properties. We determined the water uptake and proton conductivity of a large number of membranes with ϕ_v ranging from 0 to 0.49 and SL ranging from 17 to 72%. The complete data set are presented in the Supporting Information (Figures S3 and S4). Figure 9a shows water uptake, WU, of S-SES membranes equilibrated in liquid water, as a function of ϕ_v, at two fixed sulfonation levels: SL = 30% (squares) and SL = 55% (circles). In both cases, WU increased monotonically with increasing ϕ_v. At SL = 30%, WU increased from 95% at ϕ_v = 0 to 240% to ϕ_v = 0.49. At SL = 55%, WU increased from 170% at ϕ_v = 0 to 520% at ϕ_v = 0.49. The proton conductivity, σ, in contrast to WU, did not show a monotonic trend with increasing ϕ_v, as shown in Figure 9b. Instead, σ shows a peak at ϕ_v = 0.1 at both SL = 30% and SL = 55%. We have thus demonstrated that proton conductivity can be optimized by tuning ϕ_v. At low values of ϕ_v, σ increases with increasing water content. This observation is consistent with many reports in the literature.[30−33] At ϕ_v values above 0.1, σ decreases with increasing water content. We attribute this to the dilution of protons in the hydrophilic channels.[16,34]

Figure 9c shows σ as a function of λ, for S-SES membranes with SL = 30% (squares) and SL = 55% (circles). Overlaid in the same plot is proton conductivity of aqueous HCl solution[35] as a function of λ (in this case $\lambda = [H_2O]/[Cl^-]$). At low λ values, σ increases with increasing λ; above a certain λ value, σ decreases with increasing λ. This trend is seen in both S-SES membranes and HCl aqueous solutions. For HCl aqueous solutions, σ is maximized at λ = 10. (For H_2SO_4 solutions, σ is maximized at λ = 13.[36]) For S-SES membranes with SL = 30%, σ is maximized at λ = 54. For S-SES membranes with SL = 55%, σ is maximized at λ = 55. Further work is needed to establish the origin of the differences in maximum conductivity in hydrated acidic membranes and free acid solutions. It is worth mentioning that S-SES membranes with the same SL values are chemically identical. Using this fabrication method, we can systematically adjust the water uptake in these membranes and find the optimum water content that gives the highest conductivity. It is clear from our data that the optimum water content in S-SES membranes is $\lambda \approx 55$.

DOI: 10.1021/acs.macromol.5b00950
Macromolecules 2015, 48, 5648−5655

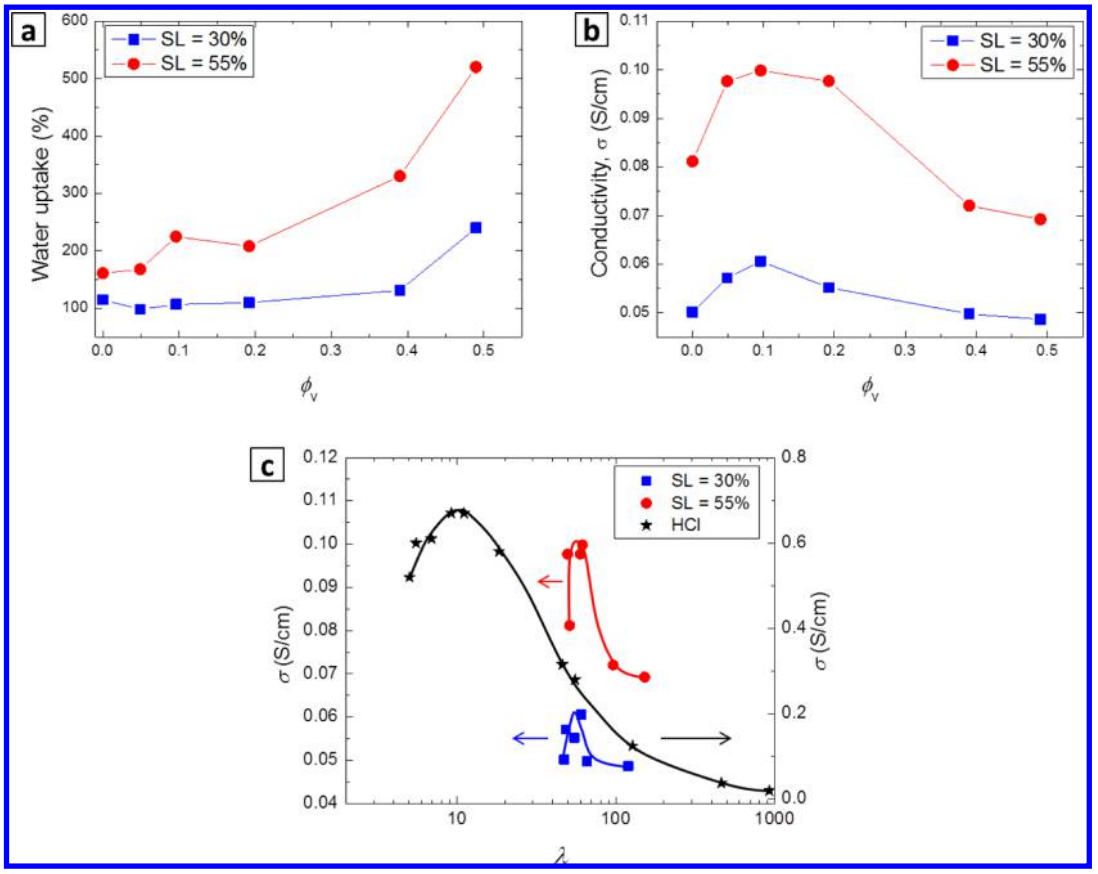

Figure 9. (a) Water uptake, WU, of S-SES membranes equilibrated in water, as a function of ϕ_v, with two fixed sulfonation levels: SL = 30% (squares) and SL = 55% (circles). (b) Proton conductivity, σ, as a function of ϕ_v, of S-SES membranes equilibrated in water, with two fixed sulfonation levels: SL = 30% (squares) and SL = 55% (circles). (c) Conductivity as a function of λ of S-SES with sulfonation levels SL = 30% (squares) and SL = 55% (circles). Proton conductivity of aqueous HCl solution as a function of λ (in this case $\lambda = [H_2O]/[Cl^-]$) is also plotted in (c) (stars). The data are taken from ref 35. Trend lines are added to guide the eye.

Additional measurements of WU and dimensional change, ΔV, of S-SES(0), S-SES(10), and S-SES(40) immersed in liquid water were made to further characterize the nature of the conducting hydrophilic microphase in our membranes. The results of these experiments are shown in Figure 10 where WU and ΔV are plotted as a function of ϕ_v. ΔV is the volume of the hydrated membrane minus of that of the dry membrane normalized by the volume of the dry membrane, defined by eq 4. The ratio of WU/ΔV, also plotted in Figure 10, is more or less independent of ϕ_v. If our membrane contained either mesoscale or macroscopic pores and immersing the membrane in water resulted in filling of the pores, then WU/ΔV would be a linear function of ϕ_v. The data in Figure 10 rules out this possibility.

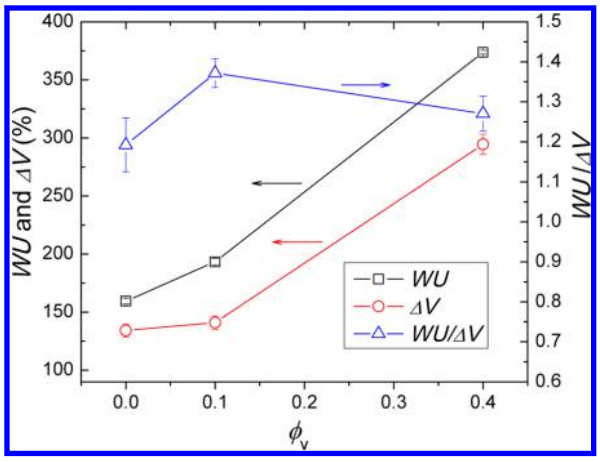

Figure 10. Water uptake, WU, dimensional change, ΔV, and WU/ΔV of S-SES membranes equilibrated in water, as a function of ϕ_v.

If sulfonation of the porous SES membranes had resulted in the complete elimination of pores, then the effect of ϕ_v on the properties of the membranes would be negligible. In contrast, the water uptake and conductivity data in Figure 9 indicate that the properties of S-SES membranes depend strongly on ϕ_v. This indicates that sulfonation does not completely eliminate pores. We are thus led to the conclusion that the size of pores in the S-SES membranes are outside the resolution of both STEM and RSoXS. We tentatively suggest that S-SES membranes contain microporous PSS domains wherein the pore size is significantly lower than that of the mesoporous PS domains in SES membranes, as depicted in Figure 1. Further work is needed to quantify the nature of the pores[37] in dry S-SES membranes that result in the properties shown in Figure 9.

CONCLUSIONS

We fabricated SES membranes with mesoscale pores lined with the PS-rich phase. The PS domains in the porous SES membranes are then sulfonated to give a porous membrane with hydrophilic and hydrophobic domains. We can tune the water uptake from 95% to 500%, by adjusting the sulfonation

DOI: 10.1021/acs.macromol.5b00950
Macromolecules 2015, 48, 5648−5655

level and ϕ_v. We found that proton conductivity did not show a monotonic trend as a function of water content. Instead, it maximizes at $\lambda \approx 55$. STEM and RSoXS revealed the presence of mesoscale pores in SES membranes, but not in S-SES membranes. We suspect that after sulfonation the mesoscale pores transformed into microscale pores that are below the detection limit of these techniques.

We show that the introduction of pores into the proton conducting phase provides additional control over water uptake and proton conductivity of block copolymer electrolyte membranes. Our approach could be used to design membranes for other clean-water-related technologies, such as nanofiltration and reverse osmosis. They will be explored in subsequent work.

■ ASSOCIATED CONTENT

Supporting Information

Figures S1−S4. The Supporting Information is available free of charge on the ACS Publications website at DOI: 10.1021/acs.macromol.5b00950.

■ AUTHOR INFORMATION

Corresponding Author

*E-mail nbalsara@berkeley.edu (N.P.B.).

Notes

The authors declare no competing financial interest.

■ ACKNOWLEDGMENTS

Primary funding for the work was provided by the Soft Matter Electron Microscopy Program from the Office of Science, Office of Basic Energy Sciences, Materials Sciences and Engineering Division of the U.S. Department of Energy under Contract DE-AC02-05CH11231. RSoXS experiments were performed at the Advanced Light Source (ALS), Beamline 11.0.1.2. The STEM and STEM tomography experiments were performed as user projects at the National Center for Electron Microscopy, Lawrence Berkeley National Laboratory. ALS and NCEM are DOE national user facilities and are supported by the Director, Office of Science, Office of Basic Energy Sciences, of the U.S. Department of Energy under the same contract. We thank Anthony Young for help with RSoXS experiments, Karen Bustillo and Peter Ercius for their help with STEM tomography experiments, and Nicolas Young for help with additional flux measurements on the membranes.

■ REFERENCES

(1) Hickner, M. A.; Pivovar, B. S. *Fuel Cells* **2005**, *5*, 213−229.
(2) Huskinson, B.; Marshak, M. P.; Suh, C.; Er, S.; Gerhardt, M. R.; Galvin, C. J.; Chen, X.; Aspuru-Guzik, A.; Gordon, R. G.; Aziz, M. J. *Nature* **2014**, *505*, 195−198.
(3) Geise, G. M.; Freeman, B. D.; Paul, D. R. *Polymer* **2010**, *51*, 5815−5822.
(4) Hsu, W. Y.; Gierke, T. D. *J. Membr. Sci.* **1983**, *13*, 307−326.
(5) Elabd, Y. A.; Hickner, M. A. *Macromolecules* **2011**, *44*, 1−11.
(6) Peckham, T. J.; Holdcroft, S. *Adv. Mater.* **2010**, *22*, 4667−4690.
(7) Park, C. H.; Lee, C. H.; Guiver, M. D.; Lee, Y. M. *Prog. Polym. Sci.* **2011**, *36*, 1443−1498.
(8) Athens, G. L.; Ein-Eli, Y.; Chmelka, B. F. *Adv. Mater.* **2007**, *19*, 2580−2587.
(9) Wang, X.; Yakovlev, S.; Beers, K. M.; Park, M. J.; Mullin, S. A.; Downing, K. H.; Balsara, N. P. *Macromolecules* **2010**, *43*, 5306−5314.
(10) Park, M. J.; Balsara, N. P. *Macromolecules* **2008**, *41*, 3678−3687.
(11) Park, M. J.; Nedoma, A. J.; Geissler, P. L.; Balsara, N. P.; Jackson, A.; Cookson, D. *Macromolecules* **2008**, *41*, 2271−2277.
(12) Park, M. J.; Downing, K. H.; Jackson, A.; Gomez, E. D.; Minor, A. M.; Cookson, D.; Weber, A. Z.; Balsara, N. P. *Nano Lett.* **2007**, *7*, 3547−3552.
(13) Beers, K. M.; Wong, D. T.; Jackson, A. J.; Wang, X.; Pople, J. A.; Hexemer, A.; Balsara, N. P. *Macromolecules* **2014**, *47*, 4330−4336.
(14) Chen, X. C.; Wong, D. T.; Yakovlev, S.; Beers, K. M.; Downing, K. H.; Balsara, N. P. *Nano Lett.* **2014**, *14*, 4058−4064.
(15) Wong, D. T.; Mullin, S. A.; Battaglia, V. S.; Balsara, N. P. *J. Membr. Sci.* **2012**, *394−395*, 175−183.
(16) Peckham, T. J.; Schmeisser, J.; Rodgers, M.; Holdcroft, S. *J. Mater. Chem.* **2007**, *17*, 3255−3268.
(17) Gann, E.; Young, A. T.; Collins, B. A.; Yan, H.; Nasiatka, J.; Padmore, H. A.; Ade, H.; Hexemer, A.; Wang, C. *Rev. Sci. Instrum.* **2012**, *83*, 045110.
(18) Wong, D. T.; Wang, C.; Beers, K. M.; Kortright, J. B.; Balsara, N. P. *Macromolecules* **2012**, *45*, 9188−9195.
(19) Van Krevelen, D. W.; Te Nijenhuis, K. In *Properties of Polymers*, 4th ed.; Van Krevelen, D. W., te Nijenhuis, K., Eds.; Elsevier: Amsterdam, 2009; Chapter 4, pp 71−108.
(20) Wong, D. T.; Wang, C.; Pople, J. A.; Balsara, N. P. *Macromolecules* **2013**, *46*, 4411−4417.
(21) Matsen, M. W. *Macromolecules* **1995**, *28*, 5765−5773.
(22) Whitmore, M. D.; Noolandi, J. *Macromolecules* **1985**, *18*, 2486−2497.
(23) Semenov, A. N. *Macromolecules* **1993**, *26*, 2273−2281.
(24) Shull, K. R. *J. Chem. Phys.* **1991**, *94*, 5723−5738.
(25) Leibler, L. *Makromol. Chem., Macromol. Symp.* **1988**, *16*, 1−17.
(26) Wang, C.; Lee, D. H.; Hexemer, A.; Kim, M. I.; Zhao, W.; Hasegawa, H.; Ade, H.; Russell, T. P. *Nano Lett.* **2011**, *11*, 3906−3911.
(27) Mitchell, G. E.; Landes, B. G.; Lyons, J.; Kern, B. J.; Devon, M. J.; Koprinarov, I.; Gullikson, E. M.; Kortright, J. B. *Appl. Phys. Lett.* **2006**, *89*, 044101.
(28) Teubner, M.; Strey, R. *J. Chem. Phys.* **1987**, *87*, 3195−3200.
(29) Schubert, K. V.; Strey, R.; Kline, S. R.; Kaler, E. W. *J. Chem. Phys.* **1994**, *101*, 5343−5355.
(30) Elabd, Y. A.; Walker, C. W.; Beyer, F. L. *J. Membr. Sci.* **2004**, *231*, 181−188.
(31) Elabd, Y. A.; Napadensky, E.; Walker, C. W.; Winey, K. I. *Macromolecules* **2006**, *39*, 399−407.
(32) Shi, Z.; Holdcroft, S. *Macromolecules* **2005**, *38*, 4193−4201.
(33) Tsang, E. M. W.; Zhang, Z.; Shi, Z.; Soboleva, T.; Holdcroft, S. *J. Am. Chem. Soc.* **2007**, *129*, 15106−15107.
(34) Zawodzinski, T. A.; Neeman, M.; Sillerud, L. O.; Gottesfeld, S. *J. Phys. Chem.* **1991**, *95*, 6040−6044.
(35) Cukierman, S. *Biophys. J.* **2000**, *78*, 1825−1834.
(36) Darling, H. E. *J. Chem. Eng. Data* **1964**, *9*, 421−426.
(37) Xie, W.; Ju, H.; Geise, G. M.; Freeman, B. D.; Mardel, J. I.; Hill, A. J.; McGrath, J. E. *Macromolecules* **2011**, *44*, 4428−4438.

DOI: 10.1021/acs.macromol.5b00950
Macromolecules 2015, 48, 5648−5655